Open Access Articles

X-ray computed tomography of wood-adhesive bondlines: attenuation and phase-contrast effects

The Faculty of Oregon State University has made this article openly available.
Please share how this access benefits you. Your story matters.

Citation	Paris, J. L., Kamke, F. A., & Xiao, X. (2015). X-ray computed tomography of wood-adhesive bondlines: attenuation and phase-contrast effects. Wood Science and Technology, 49(6), 1185-1208. doi:10.1007/s00226-015-0750-8
DOI	10.1007/s00226-015-0750-8
Publisher	Springer
Version	Version of Record
Terms of Use	http://cdss.library.oregonstate.edu/sa-termsofuse

Wood Sci Technol (2015) 49:1185–1208
DOI 10.1007/s00226-015-0750-8

ORIGINAL

X-ray computed tomography of wood-adhesive bondlines: attenuation and phase-contrast effects

Jesse L. Paris[1] · **Frederick A. Kamke**[1] · **Xianghui Xiao**[2]

Received: 6 July 2014 / Published online: 29 July 2015
© Springer-Verlag Berlin Heidelberg 2015

Abstract Microscale X-ray computed tomography (XCT) is discussed as a technique for identifying 3D adhesive distribution in wood-adhesive bondlines. Visualization and material segmentation of the adhesives from the surrounding cellular structures require sufficient gray-scale contrast in the reconstructed XCT data. Commercial wood-adhesive polymers have similar chemical characteristics and density to wood cell wall polymers and therefore do not provide good XCT attenuation contrast in their native form. Here, three different adhesive types, namely phenol formaldehyde, polymeric diphenylmethane diisocyanate, and a hybrid polyvinyl acetate, are tagged with iodine such that they yield sufficient X-ray attenuation contrast. However, phase-contrast effects at material edges complicate image quality and segmentation in XCT data reconstructed with conventional filtered backprojection absorption contrast algorithms. A quantitative phase retrieval algorithm, which isolates and removes the phase-contrast effect, was demonstrated. The article discusses and illustrates the balance between material X-ray attenuation and phase-contrast effects in all quantitative XCT analyses of wood-adhesive bondlines.

✉ Jesse L. Paris
jesse.paris@wilvaco.com

Frederick A. Kamke
fred.kamke@oregonstate.edu

[1] Department of Wood Science and Engineering, Wood-Based Composites Center, Oregon State University, 119 Richardson Hall, Corvallis, OR 97330, USA

[2] Advanced Photon Source, Beamline 2-BM-B, Argonne National Laboratory, Argonne, IL, USA

Introduction

X-ray computed tomography (XCT) is a nondestructive imaging technique capable of providing 3D data of the internal structures in materials. Achievable XCT image resolution ranges from the millimeter to nanometer scale depending on equipment, experimental parameters, and the size and volume of the imaged specimen (Chen et al. 2011; Graafsma and Martin 2008; Ketcham and Carlson 2001; Kinney and Nichols 1992). Although a well-established technique, micro-XCT has only recently been applied to study the structure and behavior of wood and wood-based composites (Hass et al. 2010, 2012; Kamke et al. 2014; Mannes et al. 2009a, b, 2010; Mayo et al. 2010; Modzel 2009; Modzel et al. 2011; Muszyński 2009; Paris et al. 2014; Standfest et al. 2012; Steppe et al. 2004; Trtik et al. 2007), this is the theme of the present work.

XCT involves the illumination of a specimen with penetrating X-ray radiation, and detecting the photons after they have traversed through the specimen. As the photons pass through the specimen, they interact with matter and are reduced in intensity and/or diffracted from their initial trajectory. The extent of these interactions is material dependent. When different materials are present in the same volume, they can be distinguished from each other if the spatial resolution is fine enough to identify clear material edges, and if there is sufficient contrast in the reconstructed image. Two primary contrast mechanisms are employed in XCT. The most common mechanism is absorption contrast, which exploits differences in material linear attenuation coefficients, μ, or the ability for that material to absorb or scatter penetrating X-rays. The value of μ depends on the energy of the incident X-rays and is proportional to material atomic number (Z) and density (Banhart 2008; Ketcham and Carlson 2001; Paris et al. 2014; Wildenschild et al. 2002). With absorption tomography, gray-scale reconstructed tomograms are 3D maps of relative attenuation coefficients (Banhart 2008; Ketcham and Carlson 2001; Wildenschild et al. 2002). The second mechanism is phase-contrast tomography. The basic principle in phase-contrast tomography is that a coherent beam of incident photons will undergo a phase shift, or Fresnel diffraction, at the interface between two materials with different refractive indices (Betz et al. 2007; Cloetens et al. 1997; Peele and Nugent 2008). In reconstructed tomograms, the phase-contrast effect results in paired, light/dark fringes at material edges, and the intensity of the effect will increase with distance between the specimen and detector, due to free-space propagation of the out-of-phase photon waves (Betz et al. 2007; Cloetens et al. 1997, 2002).

Phase-contrast tomography is particularly useful for differentiation between low Z materials, such as soft biological tissues, where there is little absorption contrast (Betz et al. 2007; De Witte et al. 2009; Peele and Nugent 2008). However, application of this phenomenon can be either qualitative or quantitative. The former occurs when radiographic projections are reconstructed with conventional XCT algorithms, and the edge enhancement effect helps researchers identify material boundaries. Quantitative applications of phase-contrast tomography involve the reconstruction of XCT data using various phase retrieval algorithms, where the

phase shift is identified, and resulting tomograms represent maps of relative refractive indices (Betz et al. 2007; Cloetens et al. 2002; De Witte et al. 2009; Weitkamp et al. 2011; Wu et al. 2008). Phase retrieval algorithms, however, are highly sensitive to the nature of the incident X-rays and often require a highly coherent, parallel, and monochromatic photon beam. Synchrotron X-ray sources are ideal for quantitative phase retrieval (QPR) XCT analyses. True phase-contrast imaging requires a sample to undergo multiple scans at varied specimen-to-detector distances or at multiple beam energies to isolate the phase-contrast effect (Cloetens et al. 2002; Gureyev et al. 2001; Peele and Nugent 2008). More recently, however, algorithms have been introduced which can utilize one, "defocused" XCT dataset from a single scan, which significantly shortens scan time and specimen damage due to prolonged exposure to ionizing radiation (Mayo et al. 2003, 2010; Paganin et al. 2002; Weitkamp et al. 2011).

To date, the majority of wood XCT studies have used conventional reconstruction methods, such as the filtered backprojection algorithm, and relied on absorption contrast for material identification and differentiation (Hass et al. 2010; Mannes et al. 2010; Modzel 2009; Modzel et al. 2011; Paris et al. 2014; Trtik et al. 2007). In microscale analyses, absorption contrast is typically adequate for studying anatomical cellular features in solid wood, as only two materials, air and wood cell wall, are present. At low XCT energies (<10 keV), the linear attenuation coefficient of wood cell wall material is sufficiently greater than that of air (Mannes et al. 2010; Paris et al. 2014). Additionally, a small degree of phase-contrast effects, such as those generated with small specimen-to-detector distances are tolerable, as dark fringe effects can be counted in the empty lumens and bright edge effects may be segmented as part of the wood signal. However, absorption contrast is more challenging in micro-XCT analyses of wood composites, where multiple materials, such as adhesives, are present in the volume of interest. Wood adhesives are typically organic and have a cured density similar to that of wood cell walls and therefore do not generate sufficient absorption contrast for simple gray-scale segmentation (Hass et al. 2012; Modzel et al. 2011; Paris et al. 2014). Several attempts have been made to increase adhesive attenuation coefficient by incorporating inorganic and heavy metal tags as contrast agents into the liquid adhesives (Evans et al. 2010; Modzel et al. 2011; Walther and Thoemen 2009); however, independent tag mobility, particle agglomeration, and phase separation between tag and adhesive molecules are common complications with this approach.

The present study is part of a broader project to quantify 3D adhesive penetration in wood-adhesive bondlines using synchrotron-based micro-XCT and then assess mechanical joint performance from the same, undamaged XCT specimens (Kamke et al. 2014; Paris et al. 2013). Consequently, three adhesive systems were studied, which met the following criteria: (1) formed bonds which could be mechanically tested, (2) could be imaged with micro-XCT and segmented from wood cell walls, and (3) had unique flow and mechanical properties from each other to offer variable datasets for the development and validation of a model to relate wood-adhesive penetration with composite joint performance (Kamke et al. 2014; Muszynski et al. 2013; Nairn et al. 2013; Paris et al. 2013, 2014; Schwarzkopf et al. 2013). In a previous publication, the authors demonstrated a method for successfully tagging a

phenol formaldehyde (PF) wood adhesive with iodine for quantitative XCT material segmentation while avoiding tag migration complications (Paris et al. 2014). In this paper, two other common wood-adhesive types, polyvinyl acetate (PVAc) and polymeric diphenylmethane diisocyanate (pMDI), were tagged with iodine and imaged with absorption contrast micro-XCT. This paper also discusses the impacts of phase-contrast effects on wood-adhesive XCT material segmentation.

Experimental

Adhesive formulation and bonding

The iodinated PF adhesive (IPF) was formulated according to a similar procedure as is used for commercial plywood adhesives (44 % solids); however, 100 % of the phenol component was replaced with meta-iodophenol (Kamke et al. 2014; Paris et al. 2014). A control PF was prepared with the same procedure, which contained no iodophenol.

A neat emulsion PVAc (54 % solids) was used in the preparation of a 50:50 mixture with the above IPF resin, similar to the one described elsewhere (Cao 2010). Both the neat PVAc and IPF resins were first diluted, individually, to 25 % solids with deionized water, and then, the two dilutions were vigorously hand-mixed until the resulting adhesive appeared homogeneous.

The iodinated pMDI (IpMDI) was prepared from a commercial pMDI resin (Huntsman, Rubinate 1840). The neat resin isocyanate (NCO) content (30.5 %) was first determined according to ASTM-D-5155, Method C, where the titrant was 1 N hydrochloric acid, and 200 mL instead of 100 mL anhydrous methanol was used to avoid solution turbidity (ASTM-D-5155 2010). A neat pMDI sample was then reacted with 2,4,6 triiodophenol (TIP, 97 % purity, Alfa Aesar) to convert approximately 10 % of the known NCO groups to iodine-substituted urethanes according to the following procedure. First, 10.92 g TIP was dissolved in 15.11 g (17 mL) anhydrous tetrahydrofuran (THF, EMD Millipore) and stirred at room temperature for 1 h. A small amount of insoluble material caused the resulting solution to appear hazy; however, this was assumed negligible compared to the majority of TIP which went into solution instantaneously. To complete the preparation, TIP/THF solution was added to 30.08 g of neat pMDI in a separate, round-bottom flask and reacted for 24 h at 50 °C under inert nitrogen (N_2) gas. To avoid unwanted moisture exposure, chemical and solution additions were all done with needle transfer techniques under N_2, and all glassware was completely clean and flamed dry prior to use. In a preliminary pMDI tagging trial, attempt was made to remove the THF solvent with vacuum distillation. However, this caused steep viscosity increase, which was impractical for wood-adhesive application, penetration, and bonding. Therefore, the THF solvent was allowed to remain in the final version of the liquid IpMDI adhesive.

Adhesives were applied at a common, resin-solid spread rate of 122 g/m^2 to the tangential longitudinal surfaces of freshly planed (12 mm × 50 mm × 150 mm), Douglas-fir (*Pseudotsuga menziesii,* DF), loblolly pine (*Pinus taeda*, SYP), or

hybrid poplar (*Populus deltoides* × *Populus trichocarpa*, HP) lamina. Specific bonding conditions varied between each adhesive type; however, the initial consolidation pressure for all treatments was 690 kPa. All PF composites were bonded in a 185 °C hot press for 8 min. The hybrid PVAc and IpMDI specimens were first compressed using the desired force and then clamped between steel plates. The clamped assembly was then placed in an oven for complete cure (hybrid PVAc at 150 °C for 3 h; IpMDI at 50 °C for 14 h followed by 103 °C for an additional 1 h).

Adhesive cure and elemental analysis

The tagged adhesives were analyzed to assess percent solids, powder density, and, in the case of hybrid PVAc, film morphology. PF resins and the hybrid IPF/PVAc samples were cured in an oven at 125 and 150 °C, respectively, for 3 h (Paris et al. 2014). Neat pMDI specimens, which require moisture to initiate the curing reaction (Frazier 2003), were placed in a desiccator with a beaker of deionized water, and the whole assembly was placed in a 103 °C oven for 48 h. The desiccator vacuum inlet remained open for steam and CO_2 to slowly vent, but still created a high temperature and humidified environment for pMDI cure. For IpMDI samples, the oven was first set to 50 °C for 48 h, which allowed bulk THF to slowly evaporate before increasing to 103 °C for an additional 48 h. The percent solids were determined by weight loss after curing. Cured specimens were ground into fine powders, and their specific gravity was measured according to a modified version of ASTM-D-5965, described elsewhere (ASTM-D-5965 2007; Paris et al. 2014).

Iodine concentrations for the cured adhesive powders were verified with neutron activation analysis (NAA) using the TRIGA Mk II Research Reactor at Oregon State University; reactor and NAA procedural details are provided elsewhere (Paris et al. 2014).

Iodine tag mobility was investigated in the bondlines. Specimens excised from bonded laminates were embedded in Spurr low-viscosity epoxy resin (Ellis 2006; Paris et al. 2014; Spurr 1969), and the cross section (4 mm^2) was microtomed to an ultra-smooth surface. Bondline fluorescence micrographs (FM) were collected for each specimen surface using a Nikon E400 epi-fluorescent microscope under UV light (Paris et al. 2014). The same specimen surfaces were then coated with a gold/palladium alloy and analyzed in a scanning electron microscope equipped with energy-dispersive spectroscopy (EDS) elemental mapping (Paris et al. 2014). EDS images, which were overlain elemental signatures of oxygen and iodine, provided good contrast between wood cell structure and adhesive locations. These images were then scaled and registered with the FM images for qualitative comparison (Paris et al. 2014).

Microscale X-ray computed tomography

Specimens for XCT analysis were cut from the bonded specimens using a miniature table saw and razor blade to obtain dimensions approximately 2 mm × 2 mm × 10 mm ($T \times R \times L$). The bond was centered in the XCT

specimen. End-matched specimens were retained for the ion mobility EDS experiment.

XCT scans were collected on beamline 2-BM at the Advanced Photon Source (APS), at the Argonne National Laboratory, Argonne, IL. Six total specimens were scanned for each adhesive/wood species treatment type. A total of 1501 radiographic projections were collected over 0.12° angular increments at 15.3 keV and a 250-ms exposure time. The specimen-to-scintillator distance for the majority of the APS scans was 8 mm; however, one of the loblolly pine IpMDI specimens was scanned a second time at a distance of 30 mm. Tomograms were reconstructed with a two-dimensional, Fourier-transform-based algorithm called gridrec (Dowd et al. 1999; Marone and Stampanoni 2012). The 30-mm loblolly pine IpMDI specimen data were reconstructed with a single-propagation-distance phase retrieval algorithm based on single-material assumption (Mayo et al. 2003; Paganin et al. 2002; Weitkamp et al. 2011). Software is available for phase retrieval assuming nonhomogeneous materials, but this option was not investigated (Boone et al. 2012). All reconstructed datasets were stored as longitudinal stacks of floating-point (32-bit) gray-scale, cross-sectional images with voxel side lengths of 1.45 μm. All additional XCT beamline details, acquisition parameters, and optical equipment are reported elsewhere (Kamke et al. 2014; Paris et al. 2014).

All image processing operations, for both XCT tomogram data and FM/EDS images, were done using the ImageJ-based software package Fiji, which contains several preloaded analysis plugins (Rasband 2012; Schindelin et al. 2012). Specific processing steps for preparing composite EDS images are described in detail elsewhere (Paris et al. 2014), while XCT image processing and segmentation methods followed a modified procedure to that previously presented by the authors (Kamke et al. 2014). Specific modifications are as follows: (1) sub-volumes, approximately 0.9 mm × 1.0 mm × 2.2 mm ($R \times T \times L$), were cropped from the center of the scanned specimens to omit machining defects or artifacts associated with the specimen geometry; (2) image contrast was enhanced by stretching the gray-scale histogram over the full range, with 0.4 % voxel saturation tolerance; (3) image stack was converted from 32-bit to 8-bit; and (4) specific gray-scale value criteria were used to segment the sub-volumes into the various material phases—air, bulk cell wall, cell wall penetrated by adhesive, and pure adhesive.

The criteria for segmenting the material phases were adhesive system dependent, since each adhesive had different attenuation characteristics. In the case of IPF and IpMDI, some low molecular weight components were believed to penetrate, at the nanoscale, into the wood cell walls (Frazier and Ni 1998; Jakes et al. 2013; Paris et al. 2013; Stockel et al. 2012). The specific criteria for segmentation are illustrated in the discussion of results (Figs. 3, 5, 6). Gray-scale values used for segmentation were determined as follows: (1) "air to cell wall"—beginning at the lower bound and increasing gray-scale value, set threshold where first derivative of the gray-scale histogram crossed zero; (2) "cell wall to pure adhesive"—set threshold at next occurrence of first derivative of the histogram crossed zero, when present. If no minima in the gray-scale histogram was detected at this point, and a gradual negative sloping curve continued along the remainder of the gray-scale range, then penetration of adhesive into the cell wall is assumed. In this case, threshold values

for adhesive in wood cell walls and pure adhesive are chosen when the second derivative (5-point moving average) of the histogram fell below 0.05 and 0.01 %, respectively, of the first derivative value range. A zero value in the average second derivative means the slope of the first derivative was no longer changing and that the voxels in this range (increasing gray value above upper tail of the pure wood peak) contained blend of cell wall and adhesive, which was steadily increasing in adhesive concentration. Visual observation confirmed that these voxels were always found at the interface of wood cells and bulk adhesive. The 0.05 % (cell wall to adhesive in cell wall) and 0.01 % (adhesive in cell wall to pure adhesive) criteria were chosen as a function of the first derivative value range because this could be objectively repeated between different sub-volumes or specimens of a particular adhesive type. While the threshold criteria associated with cell wall penetration were arbitrarily chosen, they were supported with visual observation and then held constant for each adhesive type.

Another method for segmentation was attempted and abandoned. A multimodal Gaussian distribution fit of the gray-scale data was attempted using the statistical package R (Benaglia et al. 2009). Convergence of the normalmixEM algorithm in the mixtools package of R could not be achieved on all treatments, and those that did converge produced results that were inconsistent with visual observations.

Results and discussion

Tag efficacy and adhesive X-ray attenuation

Cao (2010) had previously demonstrated compatible hybrid adhesive with various PF/PVAc ratios. A 50:50 mixture of the IPF and PVAc systems was prepared as it offered high concentration of iodine and yet maintained flow and mechanical properties different from the pure IPF system. It was observed that upon mixing the two systems, the viscosity raised much higher than both pure systems, even at the reduced solid content (25 %). Additionally, the resulting hybrid adhesive had poor dry-out resistance and thus needed to be bonded within several minutes of mixing. This behavior was different than previously observed (Cao 2010), but was believed to be due to large pH differences between the pure systems or polymer entanglements, as IPF had a very high molecular weight (Cao 2010; Paris et al. 2014). In spite of these odd liquid-state properties, cured samples of the hybrid PVAc system showed excellent film formation and coalescence, with no evidence of phase separation or polymer incompatibility.

The IpMDI specimen was prepared by reacting a sample of a commercial pMDI with 2,4,6 tri-iodophenol. Isocyanate groups readily react with phenol molecules to form urethane linkages (Frazier 2003), and with triiodophenol, three iodine atoms could be attached for each displaced isocyanate. In this case, the addition of 24 wt% iodine reduced the isocyanate content from 31 to 20 %, which is still well above that for commercial polyurethane wood adhesives, so adequate bond performance was still to be expected (Hosen 2010; Ren 2010). Theoretically, only 10 % of the initial NCO groups were converted to the modified urethane structures; however, as the

liquid resin mass increased, the final NCO content was a lower percentage of the total liquid adhesive mass. Furthermore, the liquid adhesive in this case contained THF as a delivery solvent for the triiodophenol and pMDI polymers, as well as to promote a random and homogeneous distribution of the modified polymers in the presence of the untagged MDI molecules. Early attempts to remove THF from the liquid adhesive caused sharp increases in the modified system viscosity, likely because the remaining isocyanate molecules could further react with the modified urethanes (Frazier 2003). It was expected that the THF would diffuse away during the bonding process, where under bond-consolidation pressure, the viscosity increases would not be an issue. The presence of THF likely had a large impact on how the modified adhesive penetrated and bonded relative to conventional pMDI adhesives, but that was not a concern in the present project where the model development was the main focus (Kamke et al. 2014; Muszynski et al. 2013; Nairn et al. 2013).

It was vital to ensure the iodine tags remained uniformly associated with the modified adhesive polymers throughout bonding and cure. Figure 1 shows paired images of the same specimen surfaces for loblolly pine samples bonded with the hybrid PVAc and IpMDI adhesives, acquired with FM and EDS elemental analyses. In both FM images (Fig. 1a, b), the cell walls appear light blue, and embedding epoxy in the cell lumens appears darker blue. The adhesive in both cases is dark reddish-brown.

Directly comparing images Fig. 1a–c, and b–d, it is clear that the iodine tags appear uniformly distributed in the same locations as the adhesive in the FM images. Furthermore, there is no evidence of phase separation between the IPF and PVAc polymers in either image Fig. 1a or c. In Fig. 1e, it is clear that sodium migrated away from the bond and moved freely through the wood structure. This was previously observed for the pure IPF adhesive (Paris et al. 2014); although, the previous research revealed more of the sodium remained in the bondline than observed here. Perhaps the hybrid system, which had higher water content, caused the sodium hydroxide ions in the PF catalyst to more strongly disassociate in the presence of the more acidic PVAc polymers.

The contrast in the IpMDI FM image (Fig. 1b) is not as great as for the hybrid PVAc system; yet, the iodine signal still appears uniformly distributed in the darkest adhesive locations. The lower contrast in the IpMDI image is due to heterogeneous and incomplete epoxy embedding; the brightest locations in the FM image are damaged cell wall material which folded into cell lumens during microtoming. This is evident by comparing the chlorine (Fig. 1f), which was present in the epoxy embedding media, with the FM image (Fig. 1b); there was no chlorine detected in these spots, and the oxygen signal was high.

Modified and control adhesive solid content, powder density, and iodine content are provided in Table 1. The iodine content measured with NAA is compared to a theoretical value calculated for each cured adhesive based on the known formulation components and solid content. The IpMDI solid value was higher than the expected value of 69 % based on the initial amount of THF in the liquid resin, and the solid content of neat pMDI. Perhaps some residual THF did not diffuse from the samples

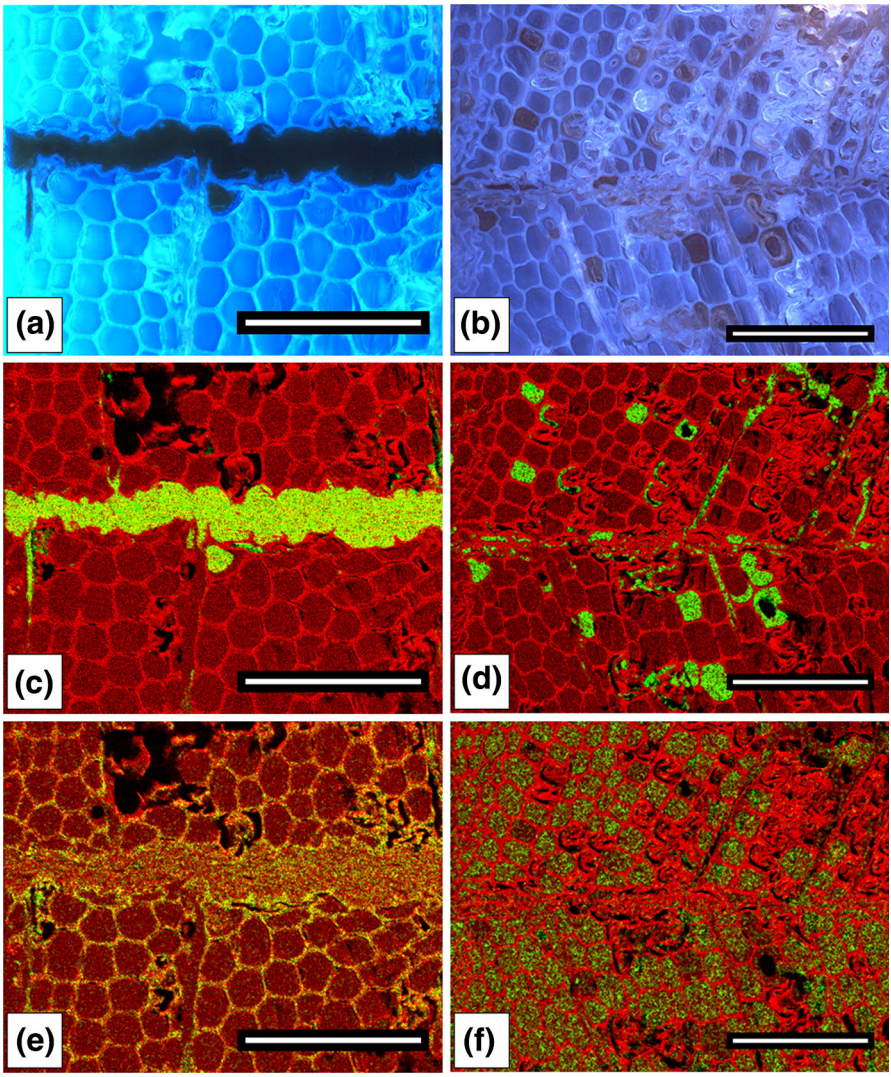

Fig. 1 Cross-sectional view of bondlines in Douglas-fir; hybrid PVAc (**a**, **c**, **e**) and IpMDI (**b**, **d**, **f**) paired by FM (**a**, **b**) and EDS (**c**–**f**) images; adhesive appears *dark* in FM images; EDS elemental signal for oxygen shown in *red*, element of interest in *green* (**c**, **d** iodine, **e** sodium, and **f** chlorine); *scale bars* 200 μm

as they were being cured, or some of the initial 27 wt% THF evaporated during the resin formulation (24 h, 50 °C, under low flowing N_2).

Cured powder density increased for all modified resins compared to controls, and IPF had significantly greater wt% iodine compared to IpMDI and the hybrid PVAc, which were approximately the same.

Absorption contrast XCT for this experiment depended on adequate difference in X-ray attenuation between the cell wall and the adhesives. Theoretical attenuation

Table 1 Average cured adhesive solid content, powder density, and iodine content; $n = 3$, standard deviation in parentheses

Adhesive	Solids (wt%)	Powder density (g/cm^3)	Cured I content (wt% I)	
			Calculated	Measured
Control PF	43.2 (1.3)	1.43 (0.06)	–	–
IPF	44.1 (0.9)	2.24 (0.06)	41.1	39.5 (0.2)
Neat pMDI	92.5 (0.1)	1.18 (0.09)	–	–
IpMDI	78.3 (0.1)	1.41 (0.06)	22.0	24.0 (0.6)
Neat PVAc	53.7 (0.1)	1.24 (0.03)	–	–
Hybrid IPF/PVAc	24.1 (0.5)	1.59 (0.09)	21.3	23.9 (0.3)

coefficients were calculated for each adhesive formulation and compared to an estimated value for cell wall substance. The linear X-ray attenuation coefficient for each adhesive can be estimated based on density and molecular structure over a broad range of possible XCT photon energies (Henke et al. 1993; Paris et al. 2014). These theorized structures and attenuation estimates are provided in Fig. 2. The structure for cellobiose is provided elsewhere and used here as an analog for the wood cell wall (Fengel and Wegener 1983). The IPF structure has been refined from that which was previously presented (Paris et al. 2014). Dimethylene ether bridges tend to release formaldehyde upon cure and revert to the more stable methylene monomer linkage (Fig. 2a; Park et al. 2002). This change did not have a significant impact on the calculated IPF attenuation behavior. Additionally, the theoretical repeat unit provided for the hybrid PVAc system is a stoichiometric combination of the IPF and PVAc dimer formulae based on the mixing ratio. Each phenol unit in the IPF adhesive contained the iodine tags, and therefore, every IPF molecule should have the same iodine concentration, independent of molecular weight. For IpMDI and the hybrid PVAc systems, this was not the case. In both of these systems, the tag distribution depended on liquid resin mixing efficiency, and any phase separation effects that could have occurred during bonding. However, there was no evidence of inhomogeneity in these adhesives seen in either the NAA or EDS results.

It is readily apparent that there is not a great difference between the attenuation coefficients for any of the control resins compared with cellobiose over this range of photon energy. IPF clearly has the greatest attenuation behavior, which is understandable as it had the greatest iodine content and density (Table 1). However, the attenuation coefficients for hybrid PVAc and IpMDI are at least an order of magnitude greater than cellobiose and are nearly indistinguishable from each other. This is not surprising as they both have similar density and iodine content. At the indicated scan energy, 15.3 keV, the three modified adhesives were predicted to offer sufficient X-ray absorption contrast to the surrounding wood cell walls. While the attenuation coefficients appear to maintain reasonable separation to still higher beam energy, the cellobiose attenuation becomes exceedingly small, indicating that the wood material would be almost transparent to the harder X-rays. Consequently, higher beam energy would force greater overlap of attenuation coefficient between the air and wood cell wall and reduce the resulting image contrast.

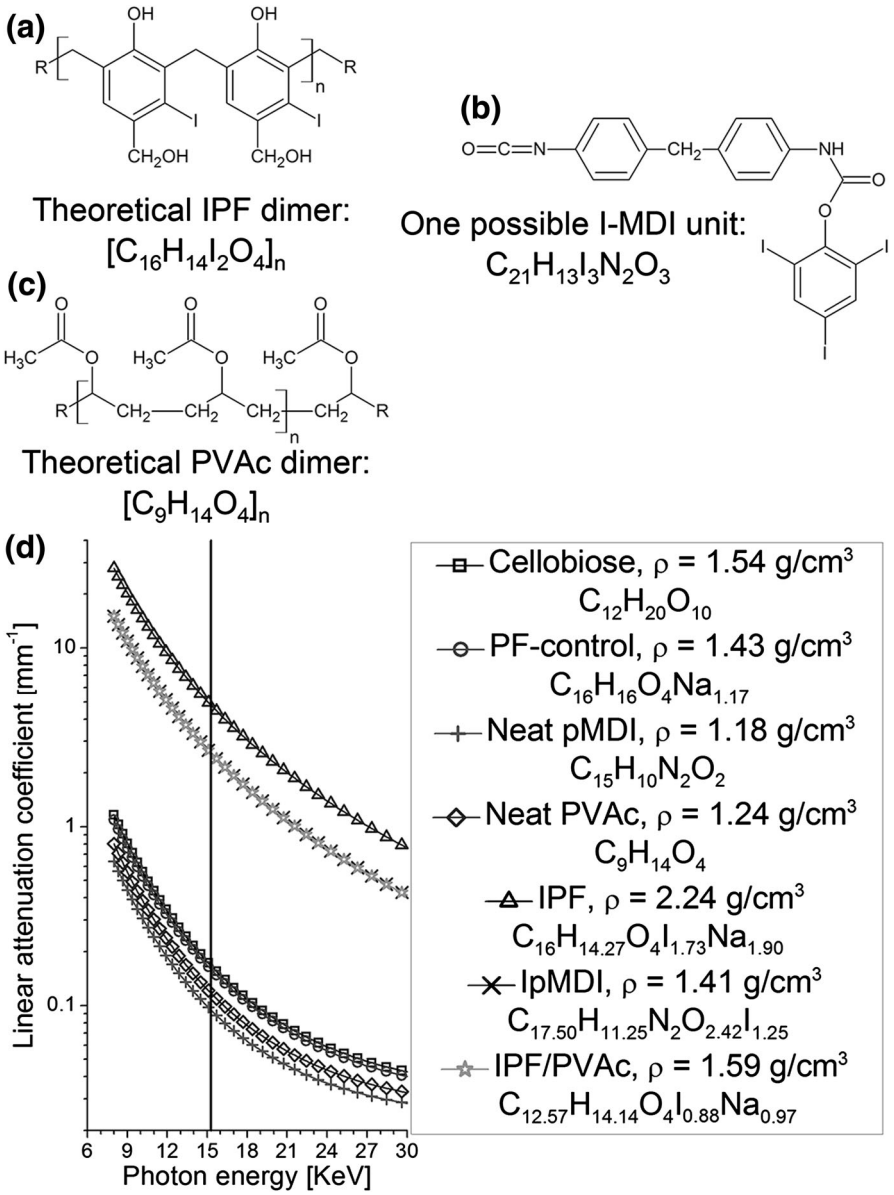

Fig. 2 **a–c** Theoretical dimer repeat units for each modified adhesive system, and **d** calculated X-ray attenuation coefficients for each cured adhesive; the legend provides the specific molecular formula and density (ρ) values used in the calculation; the *vertical line* at 15.3 keV indicates the XCT scan energy

Adhesive absorption contrast

Figures 3, 5, and 6 show reconstructed sub-volumes, as well as their corresponding gray-scale histograms and threshold values, for specimens bonded with IPF, IpMDI,

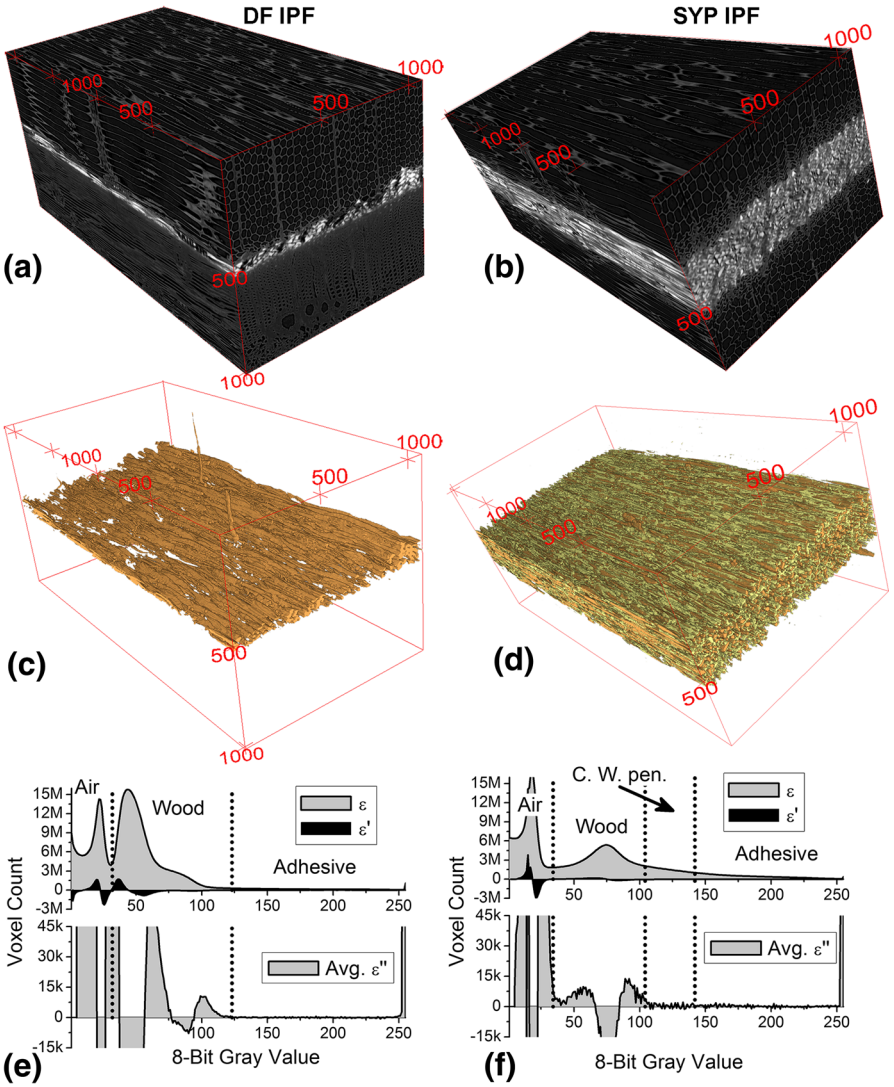

Fig. 3 IPF bonded wood shown as XCT gray-scale sub-volumes (**a**, **b**), segmented adhesive (**c**, **d**), and "trimmed" 8-bit gray-scale histograms (*top*—gray value and first derivative, *bottom*—average second derivative); species (*left*—Douglas-fir, *right*—loblolly pine); sub-volume bounding box dimensions in μm

and the hybrid PVAc adhesives, respectively. All six specimens of each treatment type showed sufficient contrast for material segmentation, but these particular specimens were chosen as they show distinctly different gray-scale histograms and thus threshold values, within the same adhesive type. Two different specimens, but same adhesive, are shown in each figure. The variability between each image pair is thus due to differences in wood anatomy. Each figure depicts a solid, gray-scale, sub-volume; the darkest regions are air, and the lightest regions are adhesive.

The mid-range gray values are cell walls. The histograms show the distribution of the gray values, denoted as ε, in each sub-volume. The first and 5-point, moving-average second derivatives of the histogram, ε' and ε'', respectively, are also plotted, as these values were used to quantitatively determine the threshold levels indicated by the vertical lines. Three threshold levels were used when adhesive was detected in cell walls.

In Fig. 3, the Douglas-fir specimen contains earlywood on one side of the bondline and latewood on the other, whereas the loblolly pine specimen has earlywood on both sides. In fact, the initial laminates for the loblolly pine specimens were carefully controlled to only have earlywood at the interface. Though the spread rate and lamination pressure were the same for both species, the loblolly pine specimen shows a far greater amount of adhesive in the bondline region. The adhesive in the Douglas-fir specimen readily flowed into the earlywood cells with large lumens, and not into the small lumens of the latewood cells. Perhaps the excess adhesive flowed laterally, to more easily penetrated regions of the bondline, outside of this particular field of view. It is also apparent that the cells surrounding the loblolly pine bondline are crushed, indicating the thin-walled earlywood cells collapsed under the consolidation pressure. The presence of the denser latewood regions probably prevented this collapse in the Douglas-fir specimen. The greater amount of adhesive and more air volume in the loblolly pine IPF specimen is also evident by the relative size of the material peaks in the histograms. The air peak in the Douglas-fir histogram is shorter than in the loblolly pine specimen, and the opposite is true for the wood peak. Additionally, the wood peaks appear to be centered at different gray values in each histogram ($\sim$40 in Douglas-fir, and 75 in loblolly pine); however, this is an artifact caused by phase-contrast effects at the cell wall edges.

The shoulder to the right of the Douglas-fir wood peak is a bright phase-contrast effect. Paired light/dark fringes appear at the interface between materials with different index of refraction (Betz et al. 2007; Cloetens et al. 1997; Gureyev et al. 2001; Mayo et al. 2003). Figure 4 shows an earlywood and latewood regions on a slice from the Douglas-fir IPF specimen in Fig. 3a; the top images were processed by histogram normalization, and the bottom images were processed by histogram stretching to set the "air" phase to zero. The plots in Fig. 4b show the gray-scale value along the corresponding line segments in each image.

The phase-contrast effects appear as a dark ring of pixels just to the inside (lumen side) and as a bright ring on the extreme edges, of a double cell wall. Histogram stretching forces the dark ring effects in the cell lumens to a zero gray value and allows them to be included with the "air" gray value, but the bright rings are still present on the cell edges. In earlywood regions, these bright rings overlap across the entire thickness of the double cell wall. Latewood cell edges are much thicker, so there are still voxels in the center of a double cell wall that do not show the phase-contrast effect. The lower gray-value voxels, in the center of the cell edges, are hereafter referred to as bulk cell wall. Both sides of the loblolly pine sub-volume in Fig. 3b are earlywood, and so there is no discernable peak for bulk cell wall material in the corresponding histogram. The entire "wood" peak in Fig. 3f is comprised of over-lapping phase-contrast effects (gray value $\sim$75). The "wood"

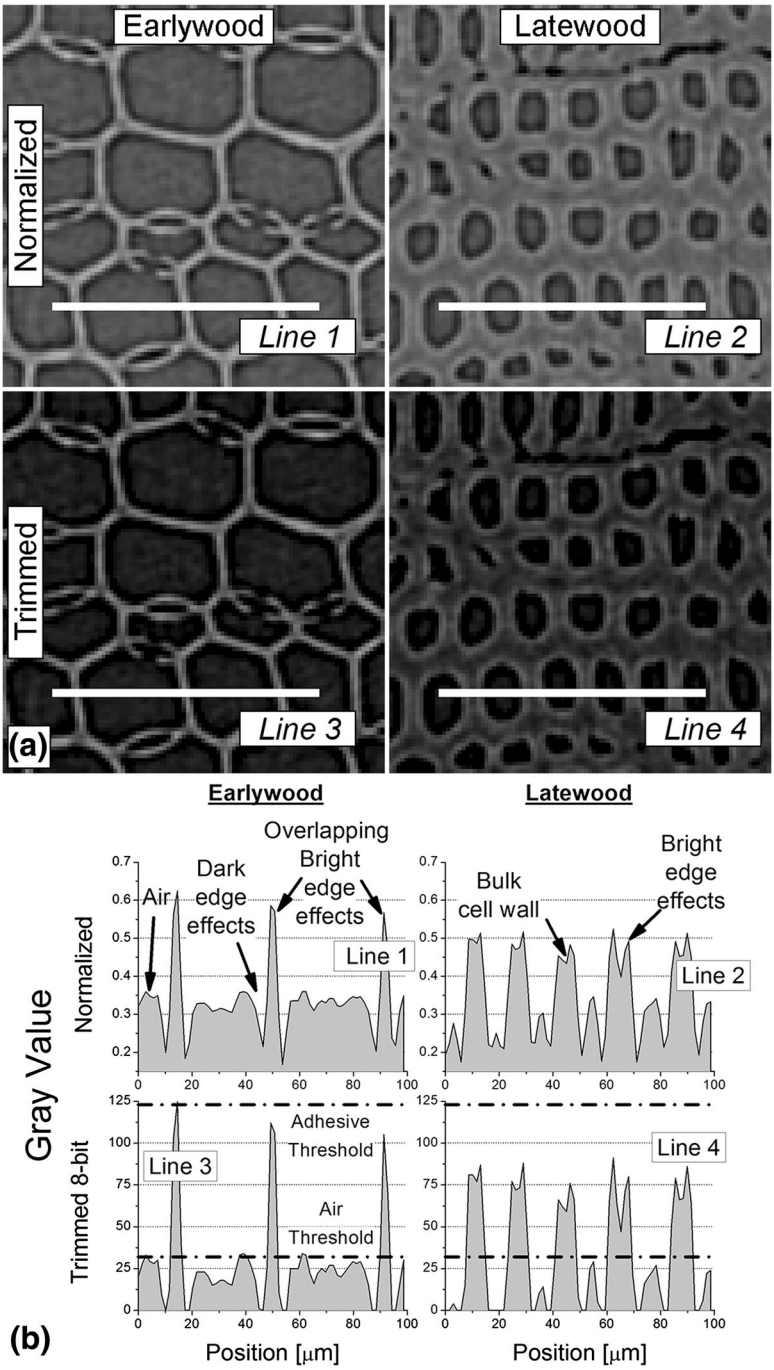

Fig. 4 **a** Cross-sectional slice from Douglas-fir IPF sub-volume in Fig. 3 showing earlywood (*left*) and latewood (*right*), after histogram normalization (*top*) and stretching (*bottom*), and **b** gray value plots corresponding to the 100-μm line segments in (**a**)

peak in the Douglas-fir laminate, however, shows both bulk cell wall (tall peak at gray value ~40) and phase-contrast effects (right shoulder at gray value ~75). The IPF, IpMDI, and hybrid PVAc adhesives were formulated to exhibit reconstructed gray levels above both the bulk cell wall and the bright phase-contrast edge effects, for the reported experimental parameters. A preliminary IPF resin, containing only 12 wt% iodine, provided a low degree of absorption contrast to the bulk cell wall, but its gray level overlapped with the bright phase-contrast effects on earlywood cell walls (Paris et al. 2014).

The Douglas-fir and loblolly pine histograms in Fig. 3 also differ to the right of the bulk cell wall/bright phase-contrast, compound "wood" peak(s). The loblolly pine histogram gradually decreases over the remaining gray levels (75 to 255), while the Douglas-fir histogram flattens out at a near zero voxel count level for the remaining gray-scale range. This is because cell wall penetration was detected in the loblolly pine sample. Cell wall penetration by phenol–formaldehyde resin was also reported in specimens studied by micro-XCT and verified by energy-dispersive spectroscopy (Paris et al. 2014). The downward bit conversion during image processing reduced the total range of gray values, which could account for some of the averaging observed in this gradient range. However, this was consistent for all specimens, and the cell wall penetration results in gray values between those for pure wood and pure adhesive. Thus, the gradient of voxel gray levels observed here is due to partial volume effects, which occur when two materials occupy the same pixel (Ketcham and Carlson 2001). The 1.45 μm per voxel side spatial resolution is too coarse to differentiate adhesive and wood polymers inside the cell wall, but when both are present in the same voxel, the assigned gray value represents an average. The segmented image in Fig. 3d shows both pure adhesive voxels (orange) and the voxels containing both adhesive and cell wall, which are collectively grouped as cell wall penetration (yellow). Similar cell wall penetration was not observed in the Douglas-fir IPF specimen. This is not to say it did not occur, but rather was not detected based on the chosen threshold level criteria.

Lastly, it is interesting to note the Douglas-fir IPF gray-scale sub-volume shows three latewood resin canals (Fig. 3a). The density and chemical nature of these natural resins are similar to those of the untagged adhesives, and thus, they could not be separated from the cell walls due to lack of absorption contrast.

The IpMDI bondlines in Fig. 5 are Douglas-fir and poplar, and neither contain latewood zones nor have extensive crushing at the interface between the two lamina. IpMDI had lower density, lower iodine content, and consequently lower predicted attenuation coefficient compared to IPF (Table 1; Fig. 2d). The gray-scale histograms show the three material peaks evenly distributed across the 256 gray levels. Increasing the relative difference in absorption contrast between the cell wall and adhesive compromises relative differences between cell wall and air on a fixed gray-scale range. Phase-contrast effects are also observed in the IpMDI specimens. The breadth of the central peak in each histogram is the result of limited spatial resolution and partial volume effects where some air, cell wall, and phase-contrast effects are all present in individual voxels, which causes a gradient of gray-scale values. The partial volume effect is also evident in regions where adhesive has

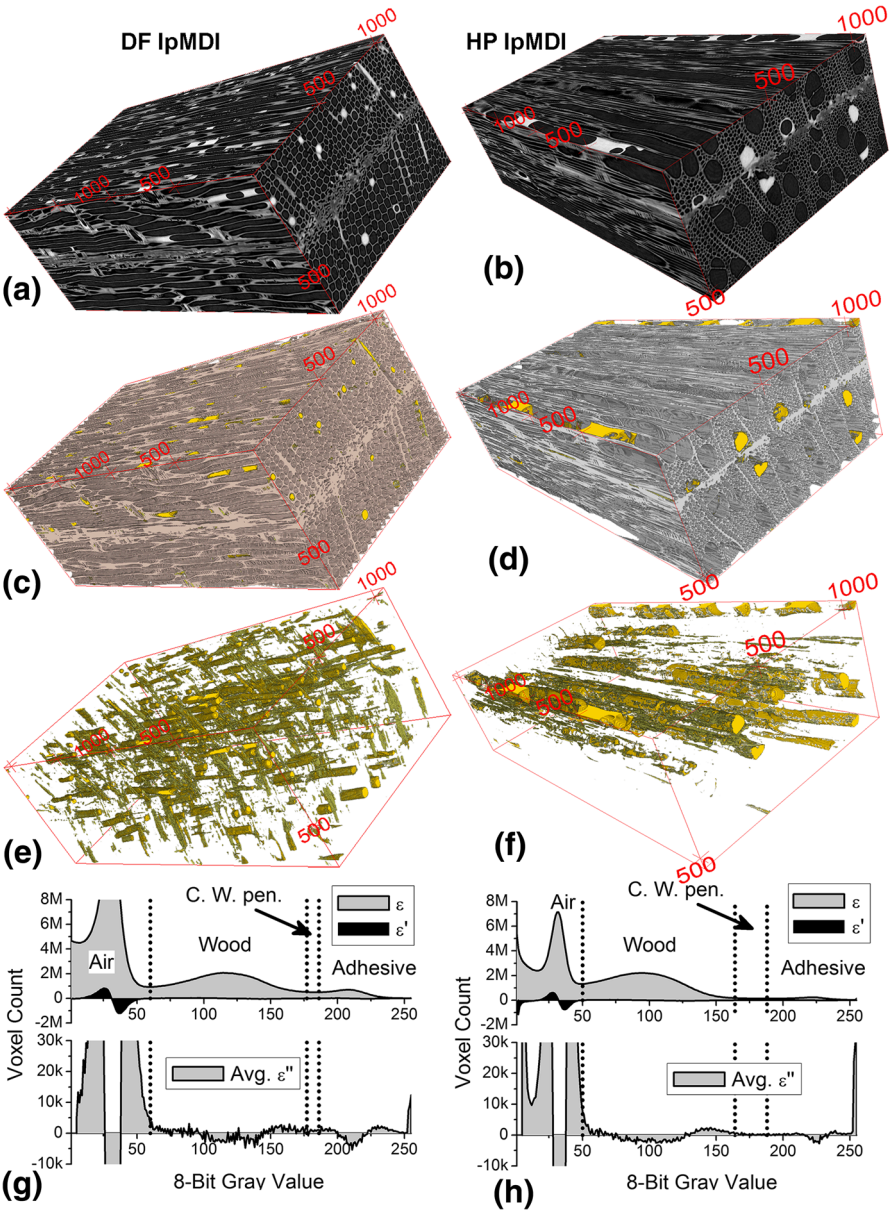

Fig. 5 IpMDI bonded wood shown as XCT gray-scale sub-volumes (**a**, **b**), segmented wood and adhesive (**c**, **d**), segmented adhesive (**e**, **f**), and "trimmed" 8-bit gray-scale histograms (*top*—gray value and first derivative, *bottom*—average second derivative); species (*left*—Douglas-fir, *right*—poplar); sub-volume bounding box dimensions in μm

penetrated the cell wall. Nevertheless, segmentation of pure adhesive (yellow) and IpMDI in the cell walls (green) was defined (Fig. 5e, f) when the moving-average second derivative fell below the 0.05 % criteria.

A segmented view of the wood structure and pure adhesive is shown in Fig. 5c, d. It appears as if there is no adhesive connecting the wood on either side of the bondline. If this was truly the case, the two halves would not remain bonded together. These IpMDI joints were capable of transferring stresses across the bondline. Therefore, adhesive must have been present between the two lamina, even if it was not detected. One possible explanation is that the IpMDI coated the cells at this interface, and the coating thickness is below the 1.45 μm per voxel XCT resolution. If this was the case, perhaps the criteria for differentiating cell wall infiltration were too strict at 0.05 %.

The hybrid PVAc adhesive was predicted to exhibit similar attenuation behavior to IpMDI (Fig. 2d). Figure 6 shows two replicate loblolly pine composite sub-volumes bonded with this hybrid system. The corresponding histograms show the material peaks are fairly evenly distributed along the 256 gray-value ranges. However, the hybrid PVAc histograms are considerably different from each other, even though they are the same wood species, adhesive, and both show only earlywood. The difference is due to the high degree of crushing near the wood/adhesive interfaces in replicate 2. The histogram for this specimen shows a shorter air peak and broader wood peak, centered at approximately 110, compared to the same wood peak in replicate 1, centered at approximately 130. The crushing forced more wood cell material into the sub-volume at the expense of airspace in the crushed cell lumens. Many of the collapsed cell walls near the bondline were in direct contact with each other. This effectively reduced the phase shift responsible for the bright edge effects seen in the other earlywood regions. One notable impact of this reduced phase-contrast effect is there was less overlapped between the wood and adhesive material peaks in replicate 2 than replicate 1. The bright edge effects in replicate 1 caused several of the cells, far from the true adhesive interface, to be included in the adhesive segmentation due to the material peak overlap (Fig. 6c). The overlap and threshold also appeared to cut off a portion of the adhesive in the center of the pure adhesive layer. Why the middle of the adhesive layer had a lower gray value than the edges is not entirely clear. Perhaps this is an indication of phase separation between the IPF and PVAc polymers; however, there was no evidence of this in neat hybrid PVAc films or in either the FM or EDS composite bondline images. This could also be the result of phase-contrast effects between wood and adhesive, which were not observed in the other resins. Other samples showed phase-contrast effects between wood and air, but not between wood and adhesive.

Quantitative phase retrieval

The adhesives, experimental parameters and segmentation criteria used in this work were able to tolerate the observed phase-contrast effects. Similar phase-contrast effects have been observed in several other XCT analyses of wood. One author noted that tyloses in oak appeared to have a greater gray-scale value than thick cell walls and argued that this was not likely due to chemical or density variations in the anatomical features (Mannes et al. 2010). This is analogous to the gray-scale differences between earlywood and latewood. In another XCT study of medium density fiberboard, air inside collapsed wood fibers had a darker gray value than

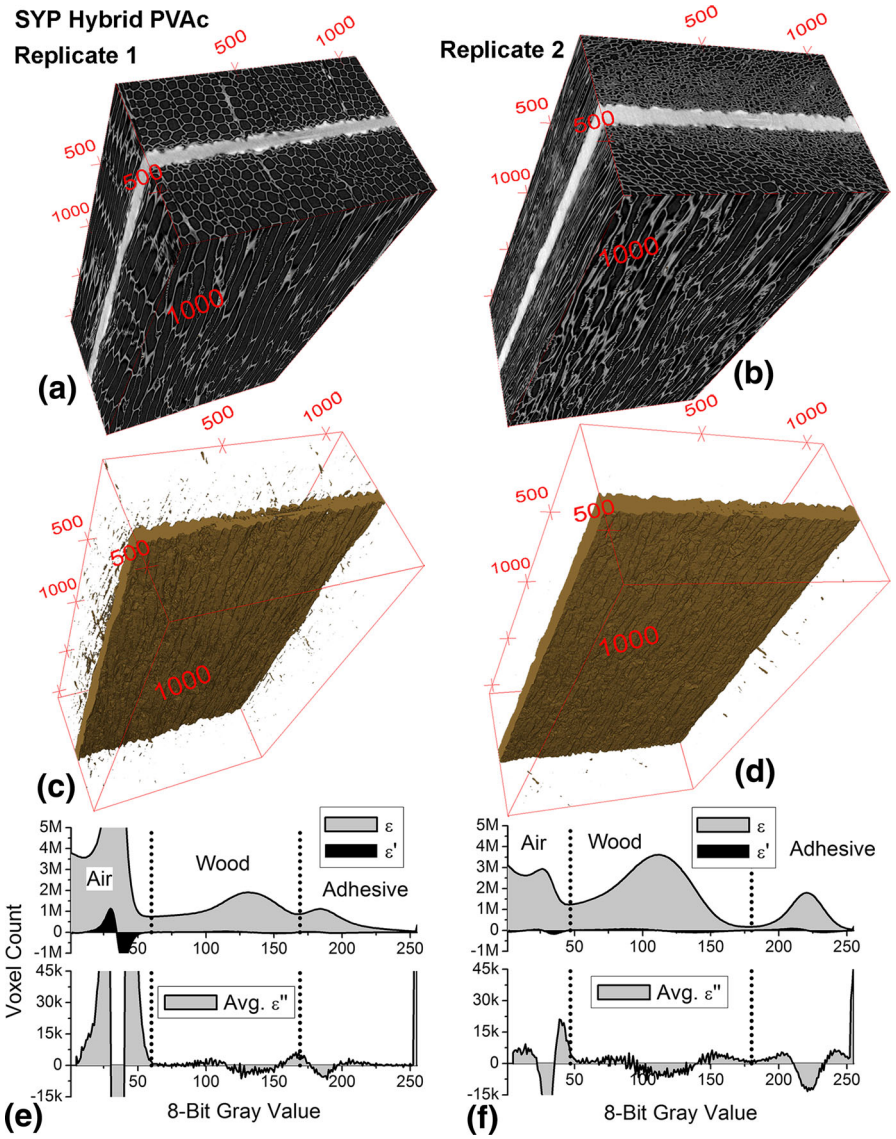

Fig. 6 Hybrid IPF/PVAc bonded loblolly pine XCT gray-scale sub-volumes (**a**, **b**), segmented adhesive (**c**, **d**), and "trimmed" 8-bit gray-scale histograms (**e**, **f**; *top*—histogram and first δ, *bottom*—true and 5 × moving average second δ); sub-volume bounding box dimensions in μm

larger pockets of air between fiber bundles (Standfest et al. 2010). This was most likely due to dark phase-contrast fringes overlapping in the smaller voids. It is also known that phase-contrast effects become stronger with larger specimen-to-detector distances (Betz et al. 2007; Cloetens et al. 1997, 2002). Modzel observed this influence in XCT scans of wood-adhesive bondline specimens when the data are reconstructed with conventional filtered backprojection algorithms, which exploit

absorption contrast effects (Modzel 2009). However, if quantitative phase retrieval algorithms are used, which capture and utilize the Fresnel phase shift effects, larger distances may be tolerated and even preferred. Figure 7 shows three views of the same location in a loblolly pine IpMDI composite, scanned and reconstructed different ways. The specimen was scanned twice at different specimen-to-scintillator distances (8 mm and 30 mm) and reconstructed with a conventional FBP algorithm and an experimental, phase-contrast QPR algorithm (Weitkamp et al. 2011).

The normalized histograms for the two FBP reconstructions show three peaks, a tall central peak and two, almost balanced lower peaks, or shoulders, on either side. The material covering the greatest area, or pixel count, is air in the cell lumens, which is the tall central peak. The next most abundant material is the cell wall, and

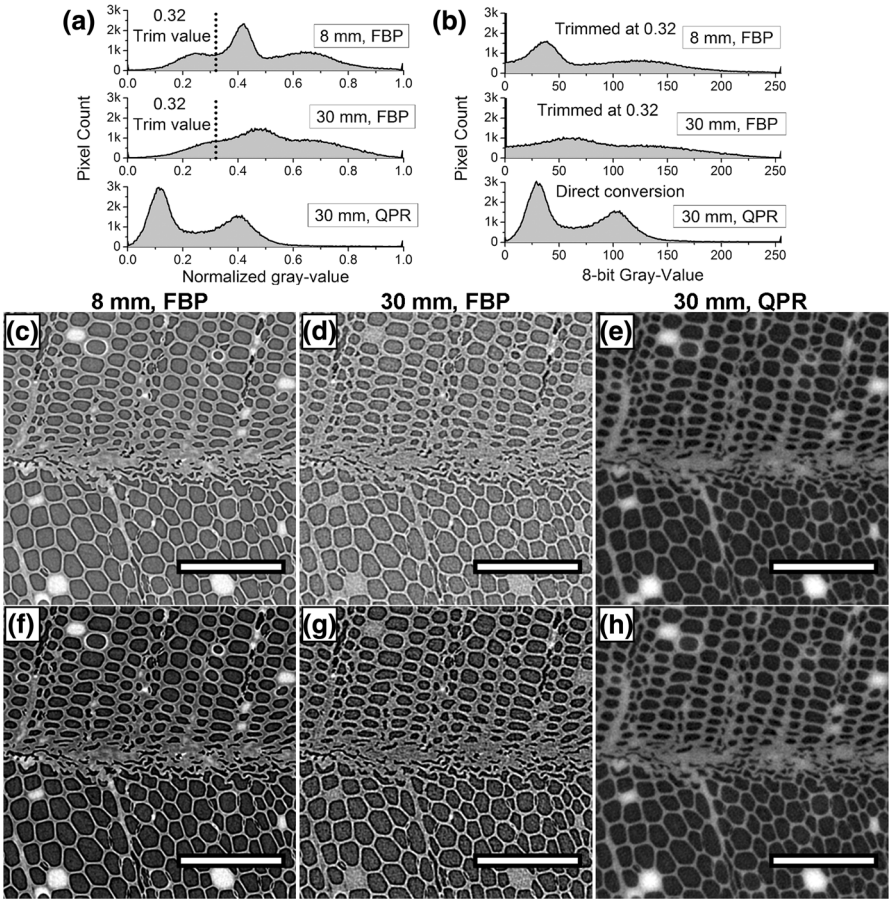

Fig. 7 Gray-scale histograms and corresponding loblolly pine IpMDI composite XCT slice (same specimen view) scanned at 8 or 30 mm specimen-to-scintillator distances, and reconstructed with an FBP or QPR algorithm; histograms: **a** normalized, and **b** trimmed at the specified value and converted to 8-bit data; images: **c**–**e** normalized, and **f**–**h** 8-bit; *scale bars* 200 μm

this corresponds to the lighter-gray (higher attenuation) peak or shoulder to the right. However, every double cell wall has two zones of dark phase-contrast effects in the lumens on either side of the edge. These dark zones add up and form the left peak or shoulder, darker than air. This specimen contains only earlywood, and so all the cells have thin walls. This causes the bright edge effects to overlap, and very little of the true wood attenuation signal is observed. Therefore, the histogram side peaks, or shoulders, appear somewhat balanced. The histogram for the 30-mm scan in Fig. 7a clearly shows greater peak overlap than that for the 8-mm specimen. This is because the effect of the X-ray phase shift is stronger with greater free-space propagation after traversing through the specimen (Betz et al. 2007; Cloetens et al. 1997). With the FBP absorption contrast algorithm, the phase-contrast effect can be recognized, and perhaps used to identify interfaces. Unfortunately, phase-contrast effects may obscure other features. On the other hand, the phase retrieval algorithm uses the phase-contrast effect in the original data reconstruction. Notice how the phase effects are eliminated in the QPR histograms, and only two peaks are observed. The 8-mm FBP images look less noisy and show good contrast between air, wood and adhesive, compared to the 30-mm FBP images. However, simply reconstructing the 30-mm data with the QPR algorithm recaptures the material gray-scale contrast. The 30-mm QPR images appear defocused compared to the 8-mm FBP images, but the histogram peaks (Fig. 7b) are narrower and show less overlap. Additionally, these images have not been filtered, and median filtering would help with image sharpness and clarity while preserving material edges (Paris et al. 2014; Russ 2011; Scholz et al. 2010).

Phase retrieval algorithms are still relatively new, compared to conventional absorption contrast reconstruction algorithms, and are still being developed for various soft-tissue XCT applications (Cloetens et al. 2002; De Witte et al. 2009; Paganin et al. 2002; Peele and Nugent 2008; Weitkamp et al. 2011). Some studies have already demonstrated their effectiveness at generating contrast in various wood and fiber tomography analyses (Betz et al. 2007; Mayo et al. 2003, 2010). One recent study was even able to segment air, wood, and a low density, untagged wax in wood lumens from XCT data reconstructed with a phase retrieval algorithm (De Witte et al. 2009; Scholz et al. 2010). The QPR data shown in Fig. 7 were only a preliminary attempt to utilize this algorithm for wood-adhesive XCT data, and the IpMDI adhesive was intentionally designed for enhanced absorption contrast to wood. Perhaps with further algorithm development, and a greater understanding of the experimental trade-offs between absorption and phase-contrast phenomena, phase retrieval algorithms may allow for quantitative segmentation of untagged wood-adhesive XCT data.

Conclusion

The procedures used to formulate and tag PF, pMDI, and PVAc with iodine resulted in adhesives that showed no evidence of iodine ionic mobility in the cured bondlines. Theoretical calculation of X-ray attenuation coefficients was consistent with observed X-ray attenuation of the adhesives and wood in the tomograms.

Therefore, the iodine-tagged adhesives could be observed and segmented in the X-ray absorption tomography data.

Segmentation of adhesive from cell walls in wood was complicated by penetration of low molecular weight fractions of the adhesive into the cell wall. Penetrating the cell wall with adhesive caused mixing of phases below the spatial resolution in the XCT procedure, thus causing a partial volume effect. The partial volume effect resulted in a gradient of gray-scale in the voxels within the cell wall adjacent to adhesive-filled lumens. The resolution of 1.45 μm, and the partial volume effect, probably prevented detection of IpMDI at the bonded interface and any thin coating of IpMDI on cell lumens.

Segmentation of adhesive, cell wall, and air was further complicated by a phase-contrast effect. Phase contrast was not a problem for defining the gray-scale threshold between air and cell wall. However, phase contrast likely obscured the detection of adhesive that penetrated the cell wall, particularly in the thin-walled cells of the earlywood regions. When adhesive penetration of the cell wall occurred, defining the gray-scale threshold value between bulk cell wall and adhesive in the cell wall was subjective.

Material attenuation differences and segmentation methods must tolerate phase-contrast effects if XCT data are reconstructed with conventional absorption contrast algorithms. However, phase retrieval algorithms, which identify and eliminate phase-contrast effects, could potentially offer greater segmentation confidence and perhaps even identify material contrast in untagged wood-adhesive bondlines.

Acknowledgments Use of the Advanced Photon Source was supported by the US Department of Energy, Office of Science, Office of Basic Energy Sciences, under Contract No. DE-AC02-06CH11357. Financial support was provided by the Wood-Based Composites Center, a National Science Foundation Industry/University Cooperative Research Center; project code A-04-KA.

References

ASTM-D-5155 (2010) Standard test methods for polyurethane raw materials: Determination of the isocyanate content of aromatic isocyanates vol ASTM D 5155-10. ASTM International, West Conshohocken, PA

ASTM-D-5965 (2007) Standard test method for specific gravity of coating powders vol ASTM B 5965-02. ASTM International, West Conshohocken, PA

Banhart J (2008) Introduction. In: Banhart J (ed) Advanced tomographic methods in materials research and engineering. Oxford University Press, Oxford, NY, pp 3–18

Benaglia T, Chauveau D, Hunter DR, Young D (2009) mixtools: An R package for analyzing finite mixture models. J Stat Softw 32:1–29

Betz O, Wegst U, Weide D, Heethoff M, Helfen L, Lee WK, Cloetens P (2007) Imaging applications of synchrotron X-ray phase-contrast microtomography in biological morphology and biomaterials science. 1. General aspects of the technique and its advantages in the analysis of millimetre-sized arthropod structure. J Microsc 227:51–71

Boone MN, Devulder W, Dierick M, Brabant L, Pauwels E, Van Hoorebeke L (2012) Comparison of two single-image phase-retrieval algorithms for in-line x-ray phase-contrast imaging. J Opt Soc Am A 29:2667–2672

Cao Y (2010) Characterization of PF/PVAc hybrid adhesive-wood interaction and its effect on wood strand composites performance. MS thesis, Washington State University

Chen H-H et al (2011) Quantitative analysis of nanoparticle internalization in mammalian cells by high resolution X-ray microscopy. J Nanobiotechnol 9:14

Cloetens P, Pateyron-Salomé M, Buffière JY, Peix G, Baruchel J, Peyrin F, Schlenker M (1997) Observation of microstructure and damage in materials by phase sensitive radiography and tomography. J Appl Phys 81:5878–5886. doi:10.1063/1.364374

Cloetens P, Ludwig W, Boller E, Helfen L, Salvo L, Mache R, Schlenker M (2002) Quantitative phase contrast tomography using coherent synchrotron radiation. In: Proceedings of SPIE, pp 82–91

De Witte Y, Boone M, Vlassenbroeck J, Dierick M, Van Hoorebeke L (2009) Bronnikov-aided correction for X-ray computed tomography. J Opt Soc Am A Opt Image Sci Vis 26:890–894

Dowd BA, Campbell GH, Marr RB, Nagarkar VV, Tipnis SV, Axe L, Siddons DP (1999) Developments in synchrotron X-ray computed microtomography at the National Synchrotron Light Source. In: SPIE's international symposium on optical science, engineering, and instrumentation. International Society for Optics and Photonics, pp 224–236. doi:10.1117/12.363725

Ellis E (2006) Solutions to the problem of substitution of ERL 4221 for vinyl cyclohexene dioxide in Spurr low viscosity embedding formulations. Microsc Today 14:32–33

Evans PD et al (2010) Visualization and numerical analysis of adhesive distribution in particleboard using X-ray micro-computed tomography. Int J Adhes Adhes 30:754–762. doi:10.1016/j.ijadhadh.2010.08.001

Fengel D, Wegener G (1983) Wood: chemistry, ultrastructure, reactions. Walter de Gruyter, Berlin

Frazier CE (2003) Isocyanate wood binders. In: Pizzi A, Mittal KL (eds) Handbook of adhesive technology, 2nd edn. Marcel Dekker Inc, New York

Frazier CE, Ni JW (1998) On the occurrence of network interpenetration in the wood-isocyanate adhesive interphase. Int J Adhes Adhes 18:81–87

Graafsma H, Martin T (2008) Detectors for synchrotron tomography. In: Banhart J (ed) Advanced tomographic methods in materials research and engineering. Oxford University Press, Oxford, pp 277–302

Gureyev TE, Mayo S, Wilkins SW, Paganin D, Stevenson AW (2001) Quantitative in-line phase-contrast imaging with multienergy X rays. Phys Rev Lett 86:5827–5830

Hass P, Wittel FK, McDonald SA, Marone F, Stampanoni M, Herrmann HJ, Niemz P (2010) Pore space analysis of beech wood: the vessel network. Holzforschung 64:639–644. doi:10.1515/hf.2010.103

Hass P, Wittel F, Mendoza M, Herrmann H, Niemz P (2012) Adhesive penetration in beech wood: experiments. Wood Sci Technol 46:243–256. doi:10.1007/s00226-011-0410-6

Henke BL, Gullikson EM, Davis JC (1993) X-ray interactions: photoabsorption, scattering, transmission, and reflection at E = 50-30,000 EV, Z = 1-92. Atom Data Nucl Data Tables 54:181–342

Hosen J (2010) Fundamental analysis of wood adhesion primers. Virginia Tech

Jakes JE, Gleber S-C, Vogt S, Hunt CG, Yelle DJ, Grigsby W, Frihart CR (2013) New synchrotron-based technique to map adhesive infiltration in wood cell walls. In: Proceedings of the 36th annual meeting of the Adhesion Society, Datona Beach, FL, p 3

Kamke FA, Nairn JA, Muszyński L, Paris JL, Schwarzkopf M, Xiao X (2014) Methodology for micro-mechanical analysis of an adhesive bond using micro computed x-ray tomography and numerical modeling. Wood Fiber Sci 46(1):1–14

Ketcham RA, Carlson WD (2001) Acquisition, optimization and interpretation of X-ray computed tomographic imagery: applications to the geosciences. Comput Geosci 27:381–400. doi:10.1016/s0098-3004(00)00116-3

Kinney JH, Nichols MC (1992) X-ray tomographic microscopy (XTM) using synchrotron radiation. Annu Rev Mater Sci 22:121–152. doi:10.1146/annurev.ms.22.080192.001005

Mannes D, Niemz P, Lehmann E (2009a) Tomographic investigations of wood from macroscopic to microscopic scale. Wood Res 54:33–44

Mannes D, Sonderegger W, Hering S, Lehmann E, Niemz P (2009b) Non-destructive determination and quantification of diffusion processes in wood by means of neutron imaging. Holzforschung 63:589–596. doi:10.1515/hf.2009.100

Mannes D, Marone F, Lehmann E, Stampanoni M, Niemz P (2010) Application areas of synchrotron radiation tomographic microscopy for wood research. Wood Sci Technol 44:67–84. doi:10.1007/s00226-009-0257-2

Marone F, Stampanoni M (2012) Regridding reconstruction algorithm for real-time tomographic imaging. J Synchrotron Radiat 19:1029–1037

Mayo S, Davis T, Gureyev T, Miller P, Paganin D, Pogany A, Stevenson A, Wilkins S (2003) X-ray phase-contrast microscopy and microtomography. Opt Express 11:2289–2302. doi:10.1364/oe.11.002289

Mayo SC, Chen F, Evans R (2010) Micron-scale 3D imaging of wood and plant microstructure using high-resolution X-ray phase-contrast microtomography. J Struct Biol 171:182–188. doi:10.1016/j.jsb.2010.04.001

Modzel G (2009) Computed X-ray analysis of wood-adhesive bonds. Dissertation, Oregon State University

Modzel G, Kamke FA, De Carlo F (2011) Comparative analysis of a wood-adhesive bondline. Wood Sci Technol 45:147–158. doi:10.1007/100226-010-0304-z

Muszyński L (2009) Imaging wood plastic composites (WPCs): X-ray computed tomography. A few promising techniques, and why we should pay attention. BioResources 4:1210–1221

Muszyński L, Kamke FA, Nairn JA, Schwarzkopf M, Paris JL (2013) Integrated method for multi-scale/multi-modal investigation of micro-mechanical wood-adhesive interaction. In: Frihart CR, Hunt CG, Yan N (eds) Proceedings of the international conference on wood adhesives 2013, Toronto, ON. Forest Products Society, New York, p 16

Nairn JA, Kamke FA, Muszyński L, Paris J, Schwarzkopf M (2013) Direct 3D numerical simulation of stresses and strains in wood adhesive bondlines based on the actual specimen anatomy from X-ray tomography data. In: Frihart CR, Hunt CG, Yan N (eds) Proceedings of the international conference on wood adhesives 2013, Toronto, ON. Forest Products Society, New York, p 11

Paganin D, Mayo SC, Gureyev TE, Miller PR, Wilkins SW (2002) Simultaneous phase and amplitude extraction from a single defocused image of a homogeneous object. J Microsc 206:33–40. doi:10.1046/j.1365-2818.2002.01010.x

Paris JL, Kamke F, Nairn JA, Schwarzkopf M, Muszyński L (2013) Wood-adhesive penetration: non-destructive, 3D visualization and quantification. In: Frihart CR, Hunt CG, Yan N (eds) Proceedings of the international conference on wood adhesives 2013, Toronto, ON. Forest Products Society, New York, p 13

Paris J, Kamke F, Mbachu R, Gibson S (2014) Phenol formaldehyde adhesives formulated for advanced X-ray imaging in wood-composite bondlines. J Mater Sci 49:580–591. doi:10.1007/s10853-013-7738-2

Park B-D, Riedl B, Yoon Soo K, So WT (2002) Effect of synthesis parameters on thermal behavior of phenol–formaldehyde resol resin. J Appl Polym Sci 83:1415–1424. doi:10.1002/app.2302

Peele AG, Nugent KA (2008) Phase-contrast and holographic tomography. In: Banhart J (ed) Advanced tomographic methods in materials research and engineering. Oxford University Press, Oxford, pp 161–180

Rasband WS (2012) ImageJ, 1997–2012 edition. U. S. National Institutes of Health, Bethesda, MD. http://imagej.nih.gov/ij/

Ren D (2010) Moisture-cure polyurethane wood adhesives: wood/adhesive interactions and weather durability. Virginia Tech

Russ JC (2011) The image processing handbook, 6th edn. CRC Press, Boca Raton

Schindelin J et al (2012) Fiji: an open-source platform for biological-image analysis. Nat Methods 9:676–682

Scholz G, Zauer M, Van den Bulcke J, Van Loo D, Pfriem A, Van Acker J, Militz H (2010) Investigation on wax-impregnated wood. Part 2: study of void spaces filled with air by He pycnometry, Hg intrusion porosimetry, and 3D X-ray imaging. Holzforschung 64:587–593. doi:10.1515/hf.2010.090

Schwarzkopf M, Muszyński L, Nairn J (2013) Stereoscopic optical method for the assessment of load transfer patterns across the adhesive bond interphase. In: Frihart CR, Hunt CG, Yan N (eds) Proceedings of the International Conference on Wood Adhesives 2013, Toronto, ON. Forest Products Society, New York, p 12

Spurr AR (1969) A low-viscosity epoxy resin embedding medium for electron microscopy. J Ultrastruct Res 26:31–43

Standfest G, Kranzer S, Petutschnigg A, Dunky M (2010) Determination of the microstructure of an adhesive-bonded medium density fiberboard (MDF) using 3-D sub-micrometer computer tomography. J Adhes Sci Technol 24:1501–1514. doi:10.1163/016942410x501052

Standfest G, Kutnar A, Plank B, Petutschnigg A, Kamke F, Dunky M (2012) Microstructure of viscoelastic thermal compressed (VTC) wood using computed microtomography. Wood Sci Technol 47(1):121–139. doi:10.1007/s00226-012-0496-5

Steppe K, Cnudde V, Girard C, Lemeur R, Cnudde JP, Jacobs P (2004) Use of X-ray computed microtomography for non-invasive determination of wood anatomical characteristics. J Struct Biol 148:11–21. doi:10.1016/j.jsb.2004.05.001

Stockel F, Konnerth J, Moser J, Kantner W, Gindl-Altmutter W (2012) Micromechanical properties of the interphase in pMDI and UF bond lines. Wood Sci Technol 46:611–620. doi:10.1007/s00226-011-0432-0

Trtik P, Dual J, Keunecke D, Mannes D, Niemz P, Stähli P (2007) 3D imaging of microstructure of spruce wood. J Struct Biol 159:46–55. doi:10.1016/j.jsb.2007.02.003

Walther T, Thoemen H (2009) Synchrotron X-ray microtomography and 3D image analysis of medium density fiberboard (MDF). Holzforschung 63:581–587. doi:10.1515/hf.2009.093

Weitkamp T, Haas D, Wegrzynek D, Rack A (2011) ANKAphase: software for single-distance phase retrieval from inline X-ray phase-contrast radiographs. J Synchrotron Radiat 18:617–629. doi:10.1107/s0909049511002895

Wildenschild D, Hopmans JW, Vaz CMP, Rivers ML, Rikard D, Christensen BSB (2002) Using X-ray computed tomography in hydrology: systems, resolutions, and limitations. J Hydrol 267:285–297. doi:10.1016/s0022-1694(02)00157-9

Wu X, Liu H, Yan A (2008) Phase-contrast X-ray tomography: contrast mechanism and roles of phase retrieval. Eur J Radiol 68:S8–S12. doi:10.1016/j.ejrad.2008.04.027